Four-Objective Optimization and Multi-Physical Field Coupling Analysis of Variable-Leakage-Flux Flux-Intensifying PM Machine

Xiping Liu, Longxin Du*, Siting Zhu, and Jianwei Liang

Abstract—This article proposes a new type of variable-leakage-flux flux-intensifying permanent magnet (VLF-FIPM) machine and performs optimization and multi-physical field analysis on it. By designing leakage flux bypass and various magnetic barriers, the proposed machine has the variable-leakage-flux characteristic and reverse saliency characteristic of $L_d > L_q$. Firstly, the evolution process from the conventional interior permanent magnet (IPM) machine to the proposed machine is explained. Secondly, the output torque, torque ripple, core loss, and reverse saliency ratio of the proposed machine are optimized by multi-objective comprehensive optimization method. Then the electromagnetic performance of the optimal machine is compared with that of the initial machine and conventional IPM machine. Finally, the temperature field and stress field of the optimal machine in different states are analyzed in detail. Both theoretical results and simulation analysis verify the effectiveness of the proposed design idea and optimization of the VLF-FIPM machine.

1. INTRODUCTION

In order to cope with the environmental pollution and energy problems caused by fuel vehicles, electric vehicles (EVs) have been fully developed. Drive machine is one of the core technologies of EVs [1]. At present, the most widely used in the field of EVs is permanent magnet (PM) machine, which has a series of advantages such as high torque density and high efficiency [2, 3]. However, the constant excitation produced by PM machines often leads to non-adjustable magnetic flux, which limits the development of PM machines in high-speed applications [4]. In order to solve this problem, conventional IPM machines usually increase the d-axis flux-weakening current to weaken the air-gap flux. However, the irreversible demagnetization risk of PMs and the copper loss of the winding will increase [5].

In recent years, some scholars have proposed to add an additional excitation winding as an auxiliary excitation source to a hybrid excitation machine, which can flexibly adjust the PM flux of the machine, thereby achieving a wider speed range [6, 7]. In [8, 9], a mechanical flux-adjusting permanent magnet synchronous machine was proposed and studied. This kind of machine combines mechanical devices to adjust the internal magnetic field of the machine from a physical point of view, and the effect of flux-weakening and speed expansion is obvious. In [10–12], a variable leakage flux IPM machine is proposed and studied, which controls the leakage flux between the PM poles by using q-axis current. In the flux-weakening state, by reducing the q-axis current, the inter-pole leakage flux is increased, and the air-gap magnetic field is weakened, so the speed increases. In [13, 14], through a special rotor topology design, the d-axis inductance L_d is greater than the q-axis inductance L_q, which is called a flux-intensifying IPM machine. It can not only reduce the risk of PM demagnetization, but also expand the speed range.

In this article, in order to solve the difficulty of flux-weakening speed expansion, a new type of variable-leakage-flux flux-intensifying permanent magnet (VLF-FIPM) machine is proposed. Not only

is the speed range increased, but also the core loss in the flux-weakening state is significantly reduced. In Section 2, the characteristics of rotor structure and the condition of variable-leakage-flux are analyzed. In Section 3, a multi-objective comprehensive optimization method is used to optimize the key performance of the proposed machine [15–18]. Then the basic electromagnetic performances of the initial and optimal VLF-FIPM machine and conventional IPM machine are compared in Section 4. In Section 5, the influence of core loss on the overall temperature of the VLF-FIPM machine is considered [19]. Therefore, the temperature field of the optimal VLF-FIPM machine in the rated state and the limit flux-weakening state is analyzed and compared with the conventional IPM machine. Finally, the mechanical stress and deformation of the optimal VLF-FIPM machine at high temperature and high speed are analyzed. The conclusions are shown in Section 6.

2. MACHINE TOPOLOGY AND FEASIBLE METHOD

2.1. Machine Topology

This article proposes a permanent magnet synchronous machine with variable-leakage-flux characteristic and reverse saliency characteristic. Figure 1 shows the evolution of the rotor topology from the conventional IPM machine to the VLF-FIPM machine. First, a trapezoidal magnetic barrier is set at the edge of the rotor along the q-axis to form two leakage flux bypasses. It can not only reduce the q-axis inductance, but also provide a variable path for leakage flux under different working conditions. Secondly, the arc-shaped magnetic barrier close to the inside of the rotor can reduce q-axis inductance. The parallel magnetic barriers on both sides of the d-axis magnetic circuit can not only prevent the strong cross-coupling magnetic saturation between the d-axis and the q-axis, but also reduce torque ripple. Finally, a magnetic bridge is added between the V-shaped PMs, which can effectively increase the d-axis inductance and obtain the reverse saliency characteristic of $L_d > L_q$.
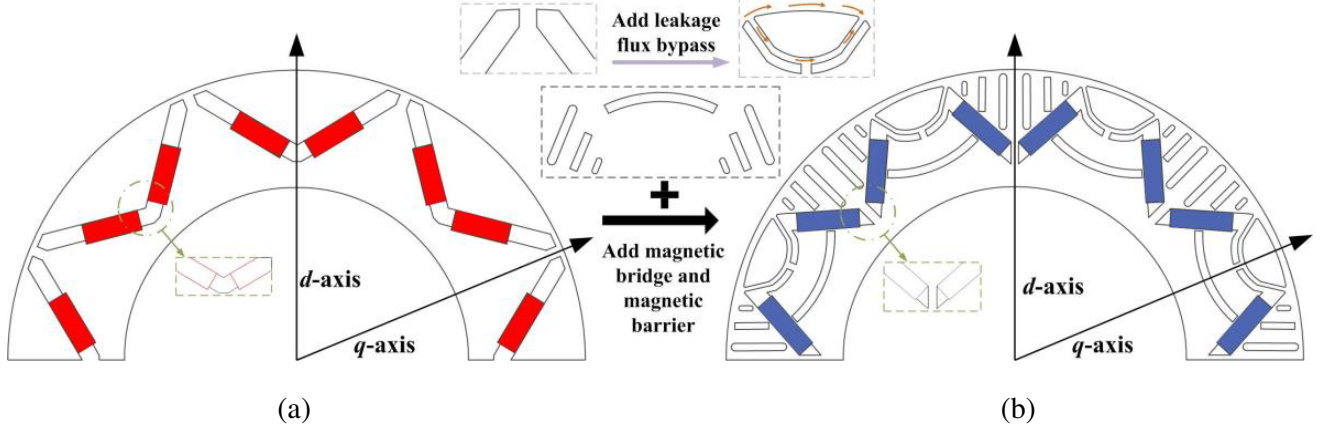

Figure 1. Rotor evolution from the conventional IPM machine to the VLF-FIPM machine. (a) Conventional IPM machine. (b) VLF-FIPM machine.

2.2. Feasible Method to Obtain the Variable-Leakage-Flux Characteristic

The VLF-FIPM machine mainly adjusts the saturation degree of leakage flux bypass by adjusting the size of the q-axis current. In the no-load state, because the permeability of the leakage flux bypass is larger than the air-gap, the PM flux will leak to the adjacent magnetic poles, forming the leakage flux, which can effectively reduce the loss in the area. In the heavy load state, the large q-axis current makes the leakage flux bypass saturated; the leakage flux disappears; the PM flux is forced into the stator to produce large torque. In the flux-weakening state, the d-axis flux-weakening current increases, the q-axis current gradually decreases; the leakage flux of the bypass increases; the PM flux decreases, which not only improves the speed, but also reduces the core loss in the flux-weakening area.
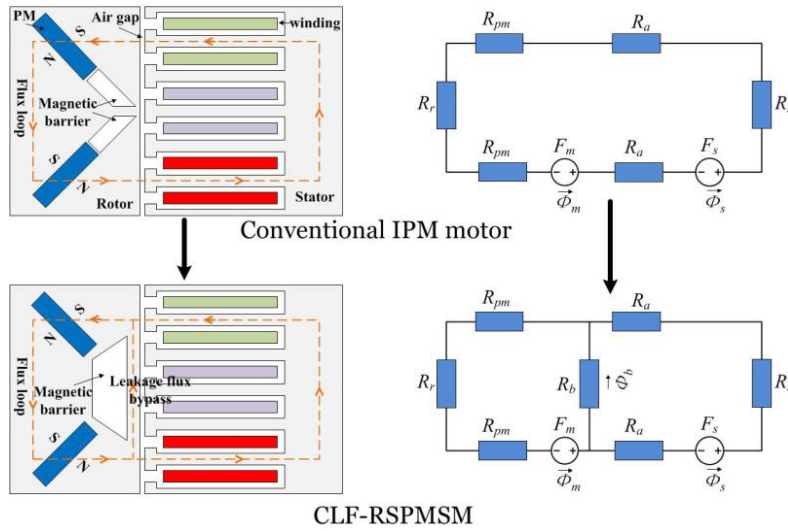
Figure 2. Flux loop evolution from the conventional IPM machine to the VLF-FIPM machine.

Figure 2 is a simplified model diagram of the evolution from the conventional IPM machine to the VLF-FIPM machine. The biggest difference between the two machines is the addition of leakage flux bypass. In the evolutionary equivalent circuit diagram, the air-gap, leakage flux bypass, rotor and stator reluctance are respectively set as R_a, R_b, R_r and R_s. R_{pm} represents the reluctance of the PM. Let the magnetomotive force of the PM be F_m. The magnetomotive force generated by the reaction force of the stator armature is set as F_s. The stator core flux is set as Φ_s, and the rotor core flux is set as Φ_m. According to the variable-leakage-flux characteristics and equivalent circuit, the formula of leakage flux Φ_b can be derived as

$$\begin{bmatrix} \Phi_s \\ \Phi_m \end{bmatrix} = \frac{1}{\det G} \begin{bmatrix} R_r + R_b + 2R_{pm} & R_b \\ R_b & 2R_a + R_b + R_s \end{bmatrix} \begin{bmatrix} F_s \\ F_m \end{bmatrix} \tag{1}$$

$$\det G = \begin{vmatrix} R_r + R_b + 2R_{pm} & R_b \\ R_b & 2R_a + R_b + R_s \end{vmatrix} = (R_r + R_b + 2R_{pm})(2R_a + R_b + R_s) - R_b^2 \tag{2}$$

Table 1. Key design parameters of the two machines.

Items	Conventional IPM machine	VLF-FIPM machine
Maximum speed (rpm)	6600	9400
PM width/thickness (mm)	16/5.6	17.4/5.1
Rated out power (kW)	10	
Slots/Poles	48/8	
Stator outer/inner diameter (mm)	269.24/161.9	
Rotor outer/inner diameter (mm)	160.4/100.64	
Rated phase current (A)	35	
Rated speed (rpm)	1000	
Turn numbers	15	
PM type	N38EH (1.26 T, 948 kA/m)	
Stack length (mm)	83.82	
Air-gap length (mm)	0.75	

$$\Phi_b = \Phi_m - \Phi_s = \frac{1}{\det G}\left[(2R_a + R_s)\,F_m - (R_r + 2R_{pm})\,F_s\right] \qquad (3)$$

When Φ_b is greater than or equal to zero, the condition for obtaining the variable-leakage-flux characteristic can be expressed by the inequality relation between F_m and F_s, as shown in Equation (4). The main design parameters of the VLF-FIPM machine are shown in Table 1.

$$\Phi_b \geq 0 \rightarrow F_m \geq \frac{R_r + 2R_{pm}}{2R_a + R_s} F_s \qquad (4)$$

3. PERFORMANCE OPTIMIZATION OF VLF-FIPM MACHINE

Figure 3 shows the corresponding flowchart of the VLF-FIPM machine performance optimization. Firstly, the initial design of the VLF-FIPM machine is determined according to the design requirements, and then the optimization objective and design variables are selected. Determine the value range of design variables according to the machine size limit and previous design experience. Sensitivity method was used to analyze the influence trend and degree of multiple design variables on the optimization objectives. The low sensitivity design variables were selected, and the single-parameter scanning method was used to obtain the optimal value. Multi-objective comprehensive optimization method was used to optimize the high sensitivity design variables. Define the optimization function and determine the optimization objective constraints. Finally, the comprehensive optimal point is selected, and the performances before and after optimization are compared.
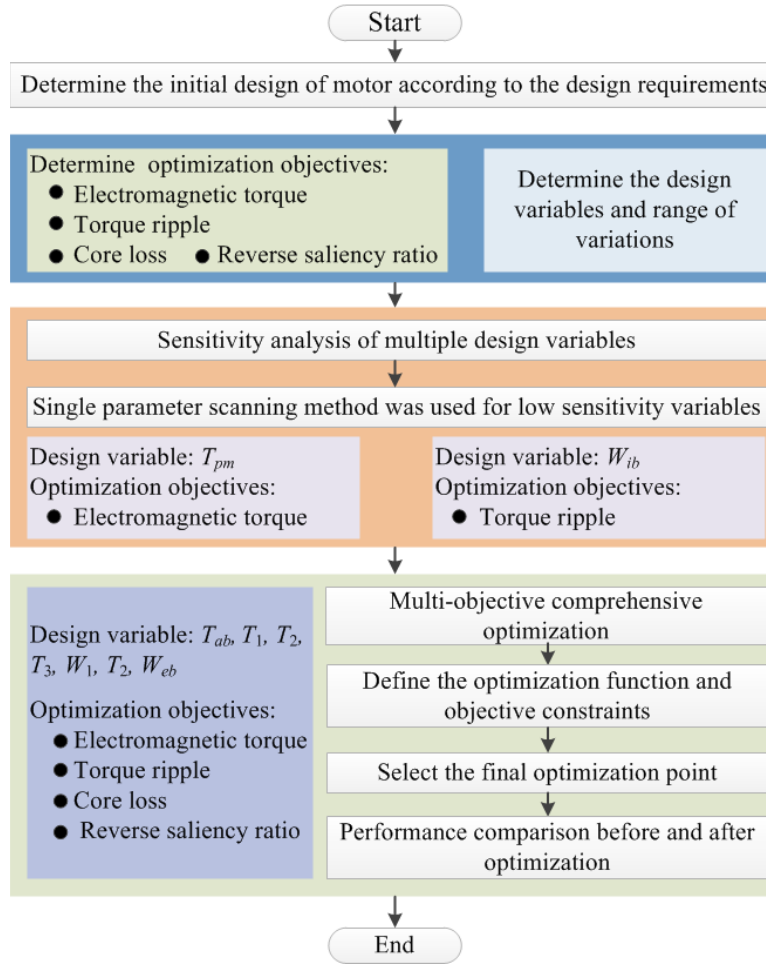

Figure 3. Optimization flowchart of the VLF-FIPM machine.

3.1. Optimization Objectives and Design Variables

The VLF-FIPM machine is mainly used in the field of electric vehicles, so relatively high output torque is essential. The more stable the electric vehicle is, the better its driving comfort will be. Therefore, torque ripple is taken as one of the optimization objectives. This paper focuses on the temperature field variation of the machine, and it is necessary to optimize the loss of the machine appropriately.

The output torque T_{out} of the VLF-FIPM machine in the d-q synchronous reference frame is described as:

$$T_{out} = \frac{3}{2}p\left[\psi_{pm}i_q + (L_d - L_q)i_d i_q\right] \tag{5}$$

where P is the pole-pair number; ψ_{pm} is the PM flux linkage; i_d and i_q are d-axis current and q-axis current, respectively.

Meanwhile, the torque ripple K_r can be expressed as follows

$$K_r = \frac{\mathrm{Max}(T_{out}) - \mathrm{Min}(T_{out})}{\mathrm{Avg}(T_{out})} \times 100\% \tag{6}$$

where $\mathrm{Max}(T_{out})$, $\mathrm{Min}(T_{out})$, and $\mathrm{Avg}(T_{out})$ are the maximum, minimum, and average values of output torque, respectively.

At the beginning of the design of the VLF-FIPM machine, the stator structure and winding form have been determined, so the copper loss generated when the winding passes through the armature current is regarded as fixed. When the VLF-FIPM machine operates at the rated condition, the eddy current loss of the PMs is far less than the core loss of the stator and rotor. Therefore, in the whole optimization process, only the core loss of the stator and rotor under the rated current is optimized. The core loss P_{Fe} can be expressed as

$$P_{Fe} = P_h + P_e + P_{ec} = fk_h B_m^\alpha + f^{1.5}k_e B_m^{1.5} + f^2 k_{ec} B_m^2 \tag{7}$$

where P_h, P_e, and P_{ec} are respectively hysteresis loss, excess loss, and eddy current loss. f is the frequency of the alternating magnetic field. k_h, k_e, and k_{ec} are respectively hysteresis loss coefficient, excess loss coefficient, and eddy current loss coefficient. B_m is the amplitude of the flux density of the stator and rotor cores, and α is the constant coefficient.

For this type of flux-intensifying machine, in order to highlight its special inductance characteristics of $L_d > L_q$, a reverse saliency ratio η_{dq} is defined as follows

$$\eta_{dq} = \frac{L_d}{L_q} \tag{8}$$

The larger the reverse saliency ratio is, the larger the positive reluctance torque is, and the corresponding output torque is. The larger d-axis inductance can also widen the speed range of the machine.

Figure 4 shows the 3D model and parameter model of the VLF-FIPM machine. Table 2 shows the variation ranges of the design parameters according to the design requirements and the limitation of the machine size.
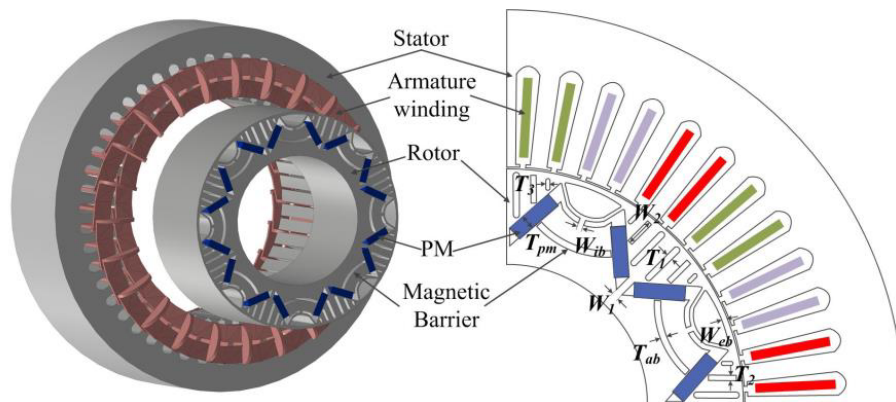

Figure 4. Parameterization of the proposed VLF-FIPM machine rotor structure.

Table 2. Design variables and variation ranges.

Design variables	Variation ranges
PMs thickness T_{pm} (mm)	[4.8, 5.2]
Medial arc barrier thickness T_{ab} (mm)	[1, 3]
1st layer parallel barrier thickness T_1 (mm)	[1.5, 3]
2nd layer parallel barrier thickness T_2 (mm)	[0.5, 2]
3rd layer parallel barrier thickness T_3 (mm)	[1, 2]
D-axis magnetic bridge width W_1 (mm)	[2, 3.4]
2nd layer parallel barrier width W_2 (mm)	[7, 9.5]
Inter-pole magnetic bridge width W_{ib} (mm)	[2, 3.5]
Edge bypass width W_{eb} (mm)	[0.5, 2]

3.2. Sensitivity Analysis and Single Parameter Scanning

In order to effectively analyze the influence of each design variable in the VLF-FIPM machine on the four optimization objectives, sensitivity analysis method is introduced in this paper. The sensitivity index $S(x_i)$ is defined as follows:

$$S(x_i) = \frac{V_{ar}\left(E\left(y/x_i\right)\right)}{V_{ar}(y)} \tag{9}$$

where $E(y/x_i)$ is the average value of the optimized objective y when the design variable x_i is unchanged; $V_{ar}\left(E(y/x_i)\right)$ is the variance of $E(y/x_i)$; $V_{ar}(y)$ is the variance of y. In addition, in order to intuitively represent the sensitivity of the design variables to the optimization objective, a radar map of the analysis results is shown in Figure 5. Due to the large number of design variables, in order to improve the overall optimization efficiency of the proposed machine, multiple design variables can be layered into the following two levels based on the sensitivity results:

Level 1: Low-sensitivity $|S(x_i)| < 0.1$

Level 2: High-sensitivity $|S(x_i)| \geq 0.1$

It can be seen from Figure 5 that the sensitivity of the design variables T_{pm} and W_{ib} to the four optimization objectives is less than 1, which means that they have a low degree of influence on the optimization objectives. For variable T_{pm}, the sensitivity to output torque is much higher than the other three optimization objectives, and the relationship between the two is positive correlation. For variable W_{ib}, the sensitivity to torque ripple is higher, and the relationship between the two is positive correlation. Therefore, the single parameter scanning method is used to optimize the low-sensitivity variables T_{pm} and W_{ib}. The optimization objectives for T_{pm} and W_{ib} are output torque and torque ripple respectively, as shown in Figure 6.
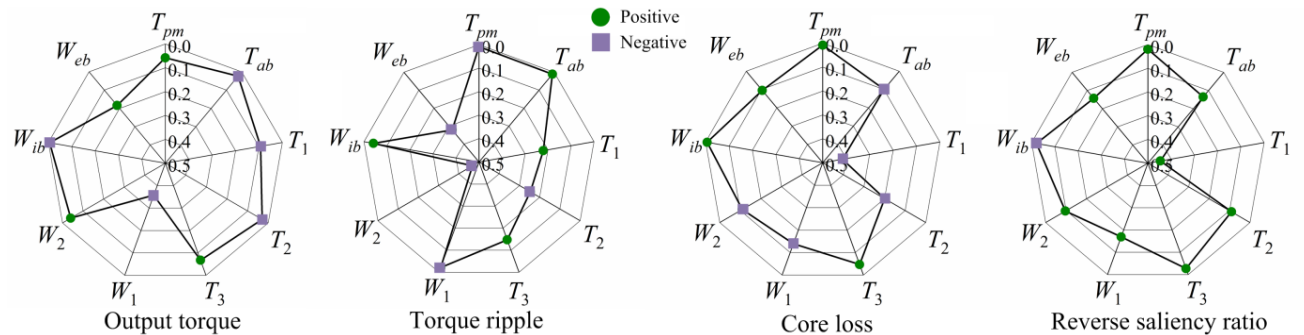
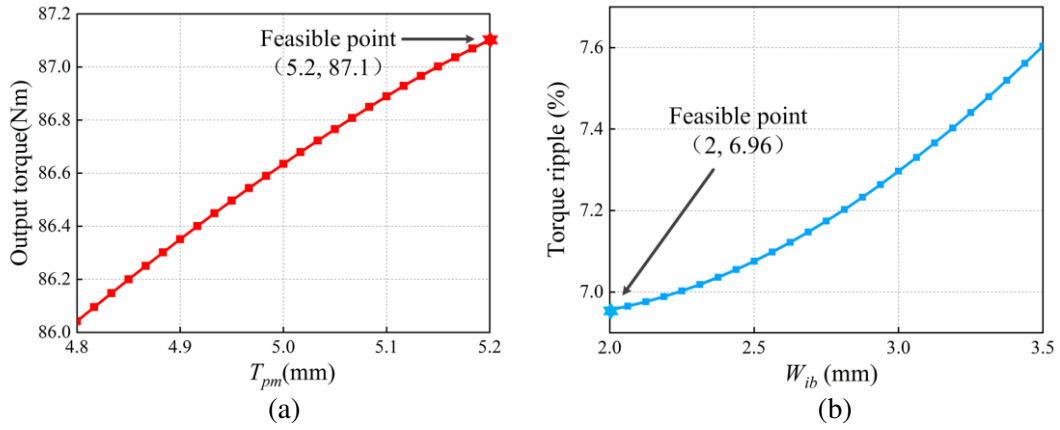**Figure 5.** Sensitivity analysis of the VLF-FIPM machine.

Figure 6. Single parameter scanning of the low sensitivity variables T_{pm} and W_{ib}. (a) T_{pm} and output torque. (b) W_{ib} and torque ripple.

As can be seen from Figure 6, the optimal values of T_{pm} and W_{ib} are 5.2 mm and 2 mm, respectively. Then perform multi-objective comprehensive optimization on the other seven high-sensitivity variables.

3.3. Multi-Objective Comprehensive Optimization

The influence trends and degrees of the seven design variables on the four optimization objectives are different. Therefore, the multi-objective comprehensive optimization method is used to carry out the tradeoff design in order to select the optimal solution. The objective optimization function $f(x_i)_{\min}$ and constraints of the VLF-FIPM machine can be expressed as:

$$\begin{cases} \text{Design variables}: T_{ab}, T_1, T_2, T_3, W_1, W_2, W_{eb}, \\ f(x_i)_{\min} = \lambda_t \dfrac{T'_{out}(x_i)}{T_{out}(x_i)} + \lambda_k \dfrac{K'_r(x_i)}{K_r(x_i)} + \lambda_p \dfrac{P'_{Fe}(x_i)}{P_{Fe}(x_i)} + \lambda_\eta \dfrac{\eta'_{dq}(x_i)}{\eta_{dq}(x_i)} \\ \text{Constraints}: T_{out} \geq 80\,\text{Nm}; \ K_r \leq 15\%; \ P_{Fe} \leq 40\,\text{W}; \ \eta_{dq} \geq 1.3 \end{cases} \quad (10)$$

where $\min x_i \leq x_i \leq \max x_i$, $i = 1, 2, 3$. λ_t, λ_k, λ_p, and λ_η are the weight coefficients of output torque, torque ripple, core loss, and reverse saliency ratio, which satisfy $\lambda_t + \lambda_k + \lambda_p + \lambda_\eta = 1$ and are assigned to
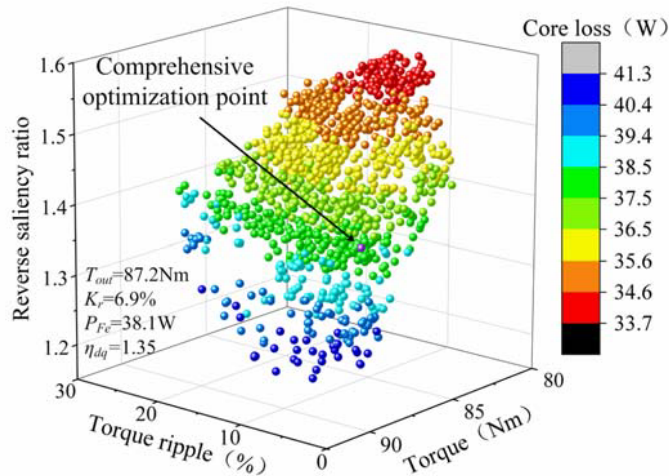

Figure 7. Optimization result of the four optimization objectives.

0.3, 0.3, 0.2, and 0.2, respectively. $T'_{out}(x_i)$, $K'_r(x_i)$, $P'_{Fe}(x_i)$ and $\eta'_{dq}(x_i)$ are the initial values of output torque, torque ripple, core loss, and reverse saliency ratio, respectively. $T_{out}(x_i)$, $K_r(x_i)$, $P_{Fe}(x_i)$, and $\eta_{dq}(x_i)$ are the optimal values of output torque, torque ripple, core loss, and reverse saliency ratio, respectively.

According to the constraint functions and conditions, a series of optimization points are presented in Figure 7, and the purple point represents the comprehensive optimal point. At the same time, the optimal values of the optimized design variables and objectives are shown in Table 3. It can be seen that the torque ripple of the VLF-FIPM machine has been significantly reduced after optimization. According to the sensitivity analysis results in Figure 5, the three design variables that have the greatest impact on torque ripple are T_2, W_2, and W_{eb}, and they are all negatively correlated. The final optimization results show that the optimal values of the three design variables are significantly increased compared to the initial values. Therefore, the torque ripple will be reduced accordingly. And the improvement of the output torque after optimization can also effectively reduce the torque ripple.

Table 3. Optimization results of design variables and optimization objectives.

VLF-FIPM machine		Initial values	Optimal values
High-sensitivity design variables	T_{ab} (mm)	2.9	2.24
	T_1 (mm)	1.66	2.14
	T_2 (mm)	1.32	1.85
	T_3 (mm)	1.36	1.44
	W_1 (mm)	2.45	2.4
	W_2 (mm)	7.6	9.5
	W_{eb} (mm)	1.4	1.7
optimization objectives	T_{out} (Nm)	86.5	87.2
	K_r (%)	19.2	6.9
	P_{Fe} (W)	40.9	38.1
	η_{dq}	1.21	1.35

4. FUNDAMENTAL ELECTROMAGNETIC PERFORMANCE COMPARISON

On the basis of the above optimization analysis, in order to further verify the effectiveness of the machine design idea and optimization method, the electromagnetic performances of the VLF-FIPM machine before and after optimization are compared in detail. Moreover, the conventional IPM machine is added for comparison, which is beneficial to the intuitive evaluation of the performance of the optimal VLF-FIPM machine.

4.1. Back-EMF and Air-Gap Flux Density

Figure 8(a) shows the no-load air-gap flux density waveform of the conventional IPM machine and the initial and optimal VLF-FIPM machines. The peak value of the air-gap flux density of the optimal VLF-FIPM machine is higher than that of the conventional IPM machine and initial VLF-FIPM machine, which indicates that the optimal VLF-FIPM machine has higher PM utilization. Figure 8(b) compares the no-load back EMF of the three machines. It can be seen that the peak back EMF of the optimal VLF-FIPM machine is higher than that of the other two machines. And the back EMF waveform of the optimal VLF-FIPM machine is high sinusoidal and symmetrical, which is conducive to machine control.

4.2. Variable-Leakage-Flux and Inductance Characteristics

Compared with the conventional IPM machine, the VLF-FIPM machine has the variable-leakage-flux characteristics and reverse saliency characteristics of $L_d > L_q$. Figure 9(a) shows the PM flux
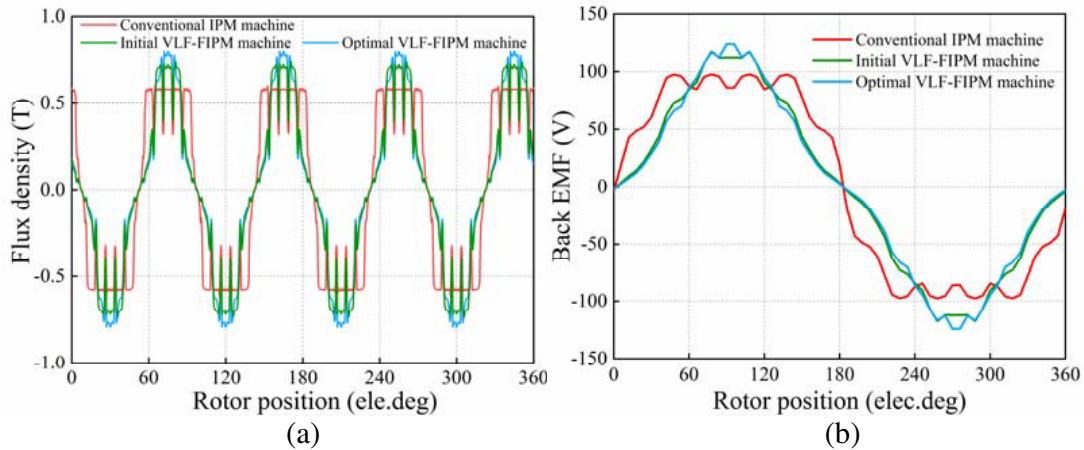
Figure 8. No-load performances of the three machines. (a) Air-gap flux density. (b) Back EMF.

distribution of the optimal VLF-FIPM machine in the no-load condition ($i_q = 0$ A). Before this, the d-axis current was set to zero, and only the q-axis current was considered, in order to avoid being affected by the stator reaction force. Under no-load condition, a large amount of PM flux flows to adjacent poles through the leakage flux bypass, forming inter-pole leakage flux. As shown in Figure 9(b), when the optimal VLF-FIPM machine runs at rated load ($i_q = 50$ A), the q-axis flux generated by the larger q-axis current makes the leakage flux bypass become saturated and blocks the PM flux to leak through the leakage flux bypass to the adjacent magnetic poles. Therefore, when the PM flux into the stator increases, the corresponding output torque increases. Figure 9(c) shows the flux distribution of the optimal VLF-FIPM machine in the flux-weakening state. On the one hand, as the q-axis current
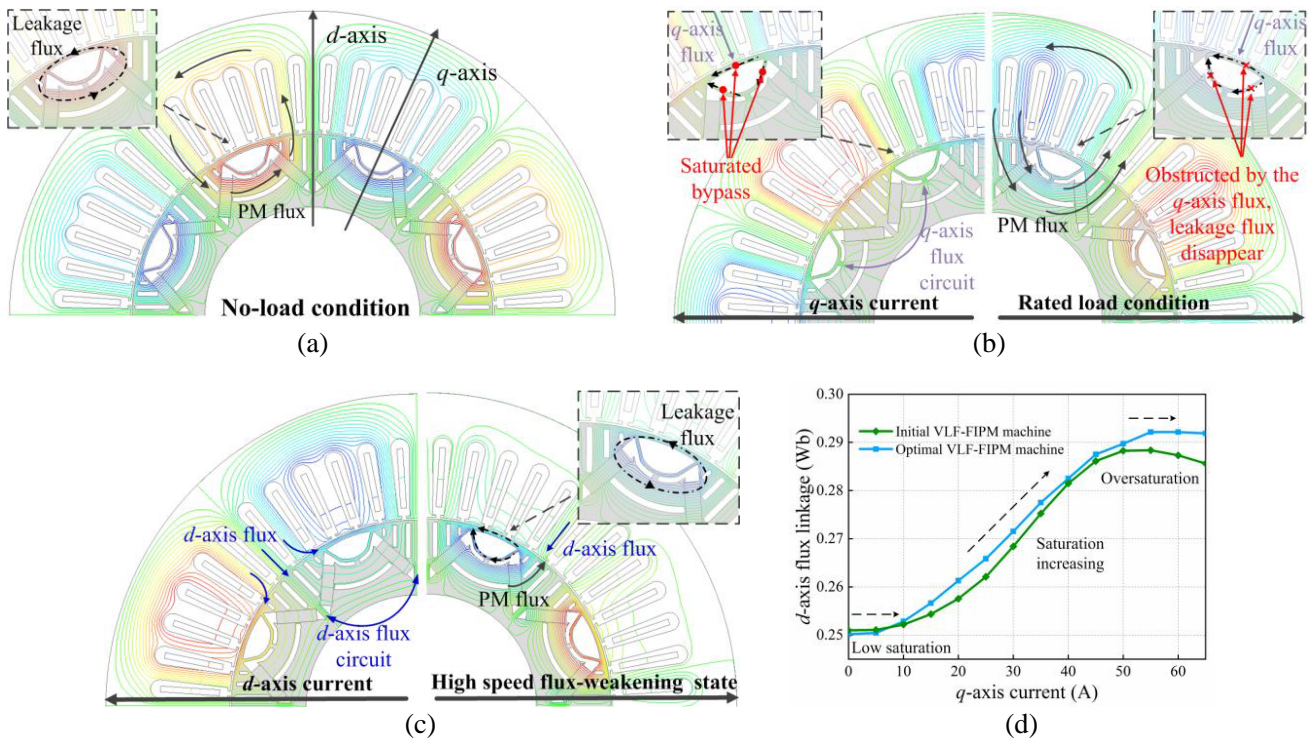

Figure 9. Flux distribution characteristics of the optimal VLF-FIPM machine. (a) No-load condition. (b) Rated load condition. (c) Flux-weakening condition. (d) Change curve of d-axis flux linkage.

decreases, the saturation degree of the leakage flux bypass decreases, and part of the PM flux leaks through the leakage-flux-bypass to the adjacent magnetic poles. On the other hand, as the d-axis current increases, a large amount of d-axis flux passes through the magnetic bridge to weaken the PM flux. Both can effectively weaken the main PM flux at the same time and expand the speed range of the machine. Figure 9(d) compares the change of d-axis flux with q-axis current of the initial and optimal machines. In the no-load state, there is more inter-pole leakage flux in the leakage flux bypass, and the d-axis flux linkage is the smallest. With the increase of the q-axis current, the d-axis flux linkage increases gradually; the saturation degree of the leakage flux bypass increases; the inter-pole leakage flux decreases gradually. When the q-axis current increases to the point where the leakage flux bypass is over-saturated, the inter-pole leakage flux disappears, and the d-axis flux linkage becomes flat. At the same time, the d-axis flux linkage of the optimal VLF-FIPM machine is smaller in the no load state and larger in the heavy load state, which means that the flux linkage variation range is better and can better meet the requirements of various working conditions of EVs.

Figure 10 shows the reverse saliency ratio η_{dq} and inductance difference $(L_d\text{-}L_q)$ of the three machines as the current amplitude $I_{\max}$ increases from $0\,\text{A}$ to $100\,\text{A}$. The reverse saliency ratio of the optimal VLF-FIPM machine is always higher than that of the conventional IPM machine and the initial VLF-FIPM machine during the whole process of current amplitude increase. In addition, the inductance difference of the conventional IPM machine is always less than zero due to $L_d < L_q$. When the current amplitude of the initial VLF-FIPM machine reaches more than $25\,\text{A}$, the inductance difference is greater than zero. The inductance difference of the optimal VLF-FIPM machine is always greater than zero, which means that the machine is always in the flux-intensifying state, which is more conducive to improving the working point of the PM.
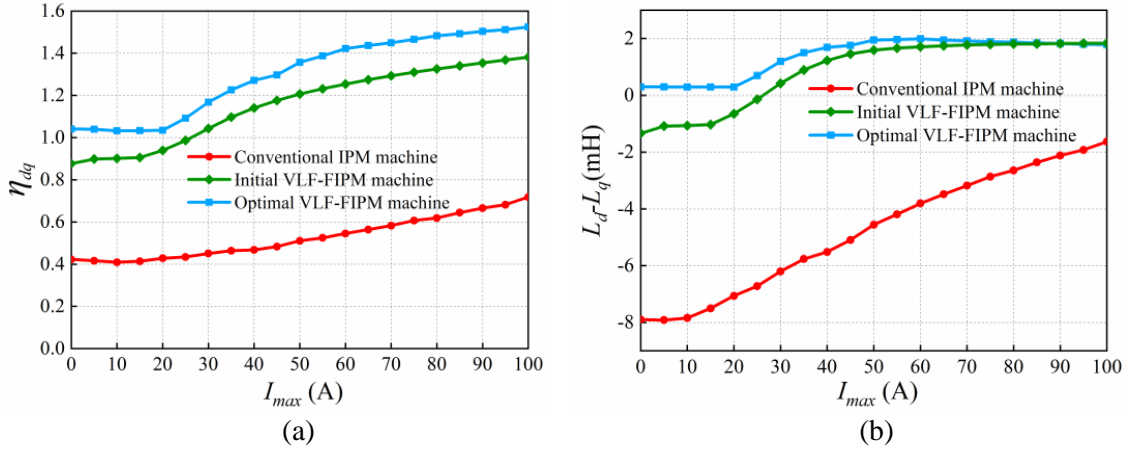

Figure 10. Inductance characteristic of the three machines. (a) Reverse saliency ratio. (b) Inductance difference $(L_d\text{-}L_q)$.

4.3. Torque and Flux-Weakening Capacity

The output torque of the three machines varies with the current angle as shown in Figure 11(a). The output torque of the conventional IPM machine reaches the maximum value of $99.2\,\text{Nm}$ at the current angle of $35°$, and the d-axis current is $-28.7\,\text{A}$, which means that the machine works in the flux-weakening region, so the irreversible demagnetization risk of the PM is greater. The initial VLF-FIPM machine achieves the maximum output torque at the current angle of $0°$. After optimization, the maximum output torque of the optimal VLF-FIPM machine is obtained at the current angle of $-5°$, and the d-axis current is $4.4\,\text{A}$, which means that the optimal machine works in the flux-intensifying region, so the operating point of the PM is improved. Meanwhile, Figure 11(b) shows the steady output torque of the three machines under the rated state. It can be seen that the output torque of the conventional IPM machine is slightly higher than that of the initial and optimal VLF-FIPM machine. However,
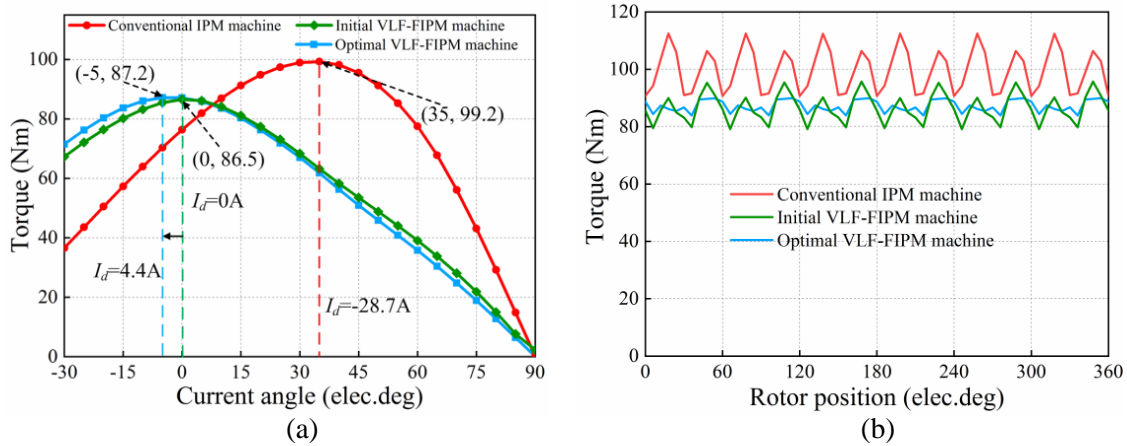
Figure 11. Torque characteristics of the three machines at the rated state. (a) Curve of torque with current angles. (b) Steady output torque and torque ripple.
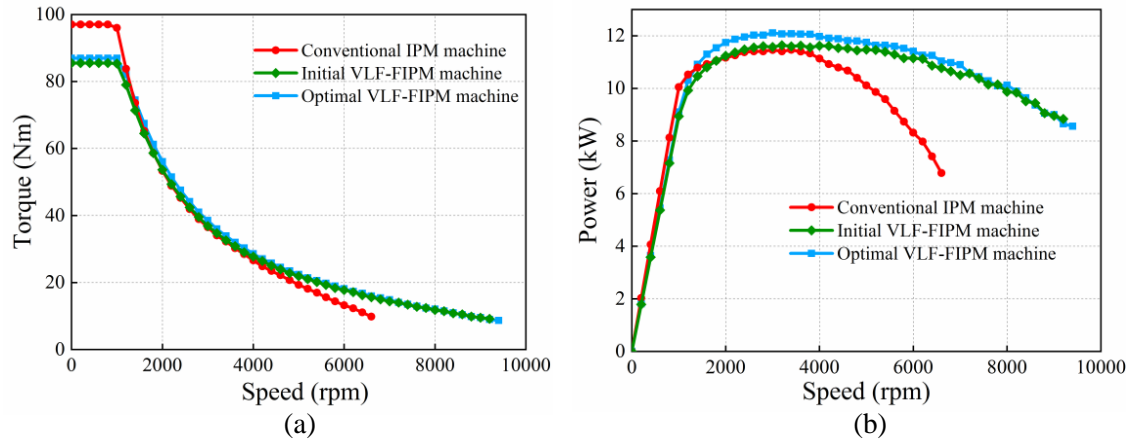

Figure 12. Flux-weakening performance comparison of the three machines. (a) Torque-speed curve. (b) Power-speed curve.

Table 4. Flux-weakening capacity parameters of the three machines.

Items	Conventional IPM machine	Initial VLF-FIPM machine	Optimal VLF-FIPM machine
Rated current (A)	35	35	35
d-axis inductance (mH)	7.2	9.6	9.7
PM flux linkage (Wb)	0.262	0.251	0.250
Characteristic current (A)	36.4	26.1	25.8

the torque ripple of the optimal VLF-FIPM machine is significantly smaller than that of the other two machines, which also proves the effectiveness of the above optimization method.

Figure 12 compares the flux-weakening performances of the three machines. The speed and constant power range of the conventional IPM machine are significantly smaller than the initial and optimal VLF-FIPM machines. On the one hand, the d-axis inductances of the initial and optimal VLF-FIPM machines are greater than that of the conventional IPM machine. On the other hand, the initial and

optimal VLF-FIPM machines have variable-leakage-flux characteristic. In the process of high-speed flux-weakening operation, the q-axis current decreases; the inter-pole leakage flux increases; the main PM flux decreases; the speed of the VLF-FIPM machine will increase correspondingly. The parameters related to flux-weakening of the three machines are shown in the Table 4.

4.4. Demagnetization Risk Analysis

The flux-intensifying effect and reverse saliency characteristic can effectively reduce the irreversible demagnetization risk of the VLF-FIPM machine. In order to verify this advantage, the irreversible demagnetization risk of the PM of the VLF-FIPM machine is analyzed in this section. Figures 13(a) and (b) respectively show the flux density distributions of the initial and optimal VLF-FIPM machines under the rated state. In addition, three observation points are selected on the PMs of the two machines respectively to study the change law of the working points of PMs under different magnetization states. As can be seen from Figure 13(c), the flux densities of the three observation points of the two machines reach the maximum in the flux-intensifying state. As the current angle increases, the flux density decreases slowly. In the limit flux-weakening state, the flux density of the two machines is not much different, and both are higher than the demagnetization limit value of $0.2\,\mathrm{T}$.

In addition, the influence of high current on the PMs of the initial and optimal VLF-FIPM machines under the rated state is also investigated, and compared with the conventional IPM machines. Figure 14 shows the flux density distribution of the three machines at 2 times the rated current. At the same time, the PMs are enlarged for easy observation, and the flux density changes of the PM center points
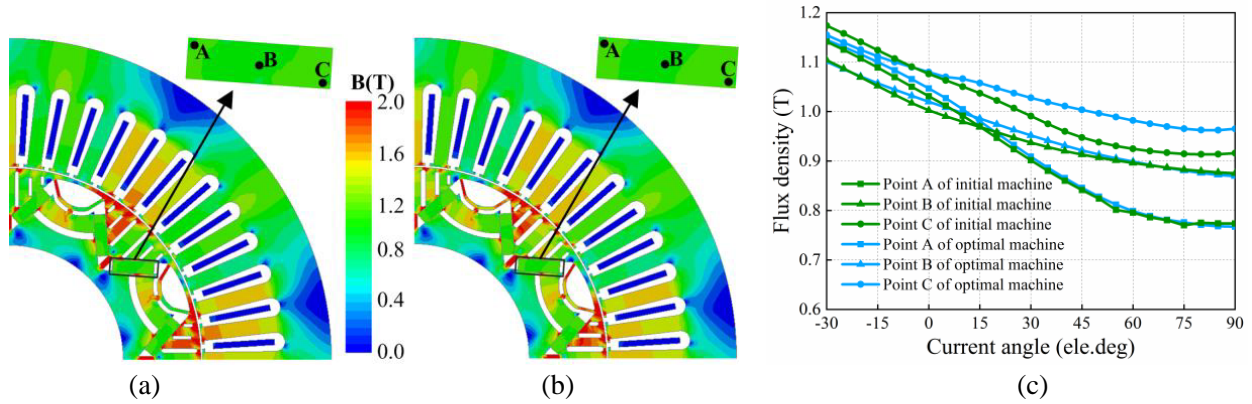

Figure 13. Flux density distribution under the rated state. (a) Initial VLF-FIPM machine. (b) Optimal VLF-FIPM machine. (c) Flux density variation of PM points of the two machines at different current angles.
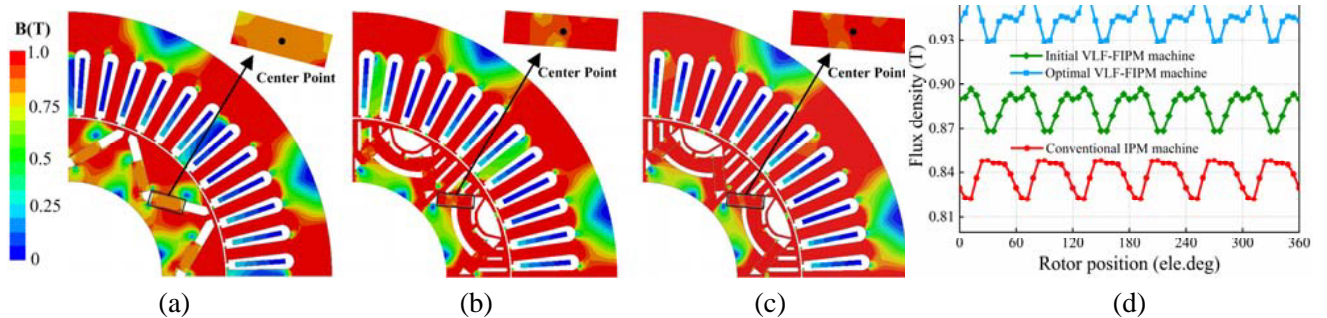

Figure 14. Flux density distribution at 2 times the rated current. (a) Conventional IPM machine. (b) Initial VLF-FIPM machine. (c) Optimal VLF-FIPM machine. (d) Flux density variation of center points of the three machines at different rotor positions.
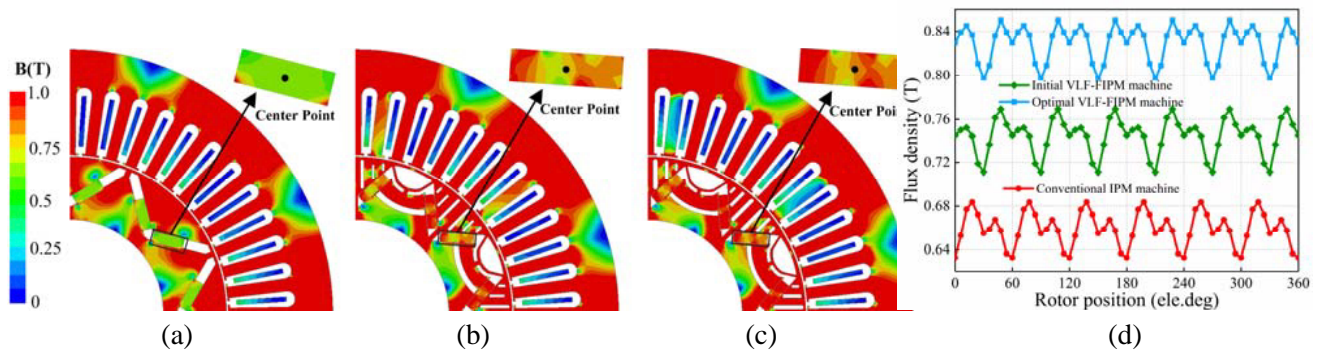
Figure 15. Flux density distribution at 4 times the rated current. (a) Conventional IPM machine. (b) Initial VLF-FIPM machine. (c) Optimal VLF-FIPM machine. (d) Flux density variation of center points of the three machines at different rotor positions.

of the three machines at different rotor positions are analyzed. It is obvious that the flux density of the PM and center point of the optimal VLF-FIPM machine is higher than that of the other two machines. Figure 15 shows the flux density distributions of the three machines at 4 times the rated current. The flux density of the PM and center point of the conventional IPM machine is the lowest, and the flux density of the optimal VLF-FIPM machine is higher than that of the initial VLF-FIPM machine, which means that the irreversible demagnetization risk of the optimal VLF-FIPM machine is lower in the flux-intensifying state.

5. TEMPERATURE FIELD AND STRESS FIELD

5.1. Loss Comparison

Figure 16 shows the core loss distribution and variation curves of the three machines at the rated state. The peak value of core loss distribution of the VLF-FIPM machine is smaller than that of the conventional IPM machine. The average core loss of the VLF-FIPM machine in the rated state is reduced from 40.9 W before optimization to 38.1 W after optimization, which is less than that of the conventional IPM machine. The optimization effect of core loss is small, mainly because multiple optimization objectives need to be considered in the optimization process, and tradeoff design is carried out.
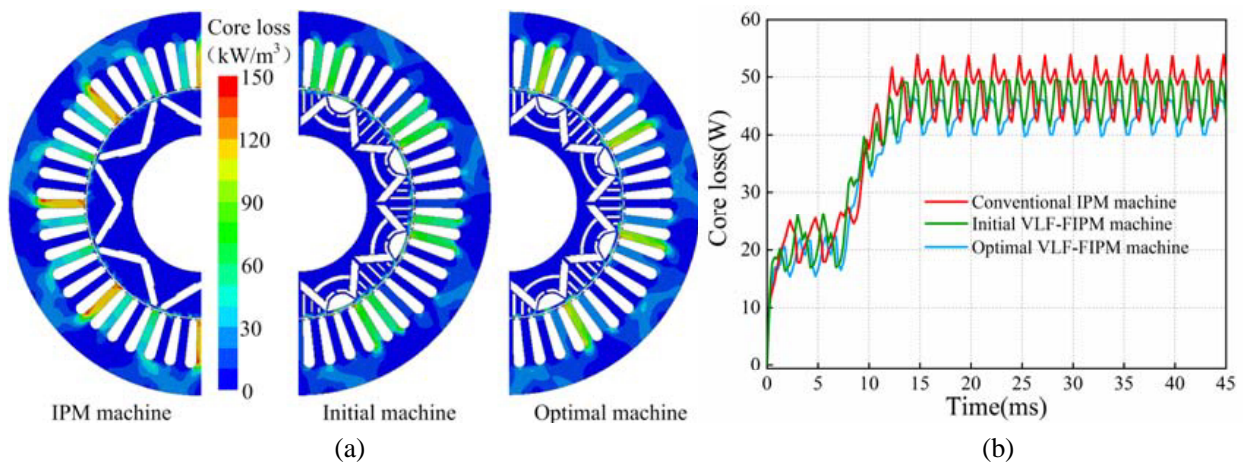

Figure 16. Core loss distribution and variation curves of the three machines at the rated state. (a) Core loss distribution. (b) Core loss curve.

Figure 17 shows the copper loss distributions of the three machines in their full speed range. It can be seen that the copper loss values of the three machines in the high torque area are not much different, because the stator and winding settings of the three machines are the same, and the rated current applied is the same. Figure 18 shows the core loss distributions of the three machines in their full speed ranges. In the limit flux-weakening state, the core loss of the conventional IPM machine is 341 W at the maximum speed of 6600 rpm; the core loss of the initial VLF-PM machine is 134.5 W at the maximum speed of 9200 rpm; the core loss of the optimal VLF-FIPM machine is only 69.1 W at the maximum speed of 9400 rpm. This is because the VLF-FIPM machine will have a large amount of inter-pole leakage flux in the flux-weakening state, thus effectively reducing the eddy current loss and hysteresis loss inside the proposed machine. This also means that the temperature of the VLF-FIPM machine in the full speed range is lower than that of the conventional IPM machine.
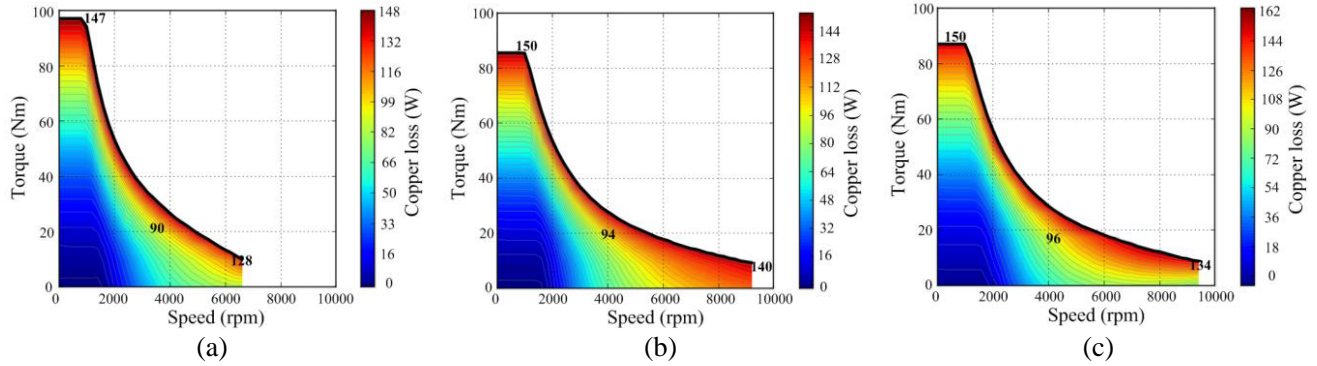

Figure 17. Comparison of copper loss map. (a) Conventional IPM machine. (b) Initial VLF-FIPM machine. (c) Optimal VLF-FIPM machine.
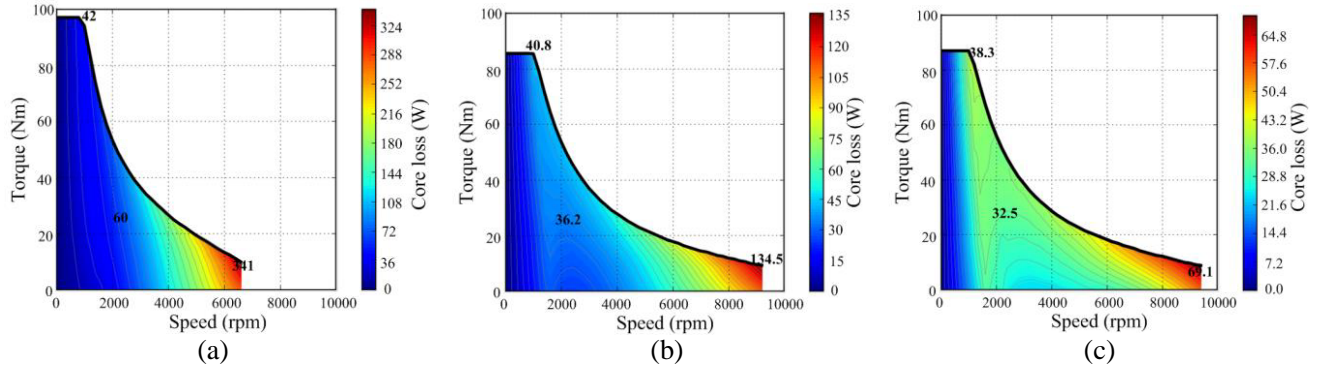

Figure 18. Comparison of core loss map. (a) Conventional IPM machine. (b) Initial VLF-FIPM machine. (c) Optimal VLF-FIPM machine.

5.2. Temperature Field

Firstly, since the effect of core loss of the VLF-FIPM machine before and after optimization is relatively small, this section focuses on analyzing the temperature field of the conventional IPM machine and optimal VLF-FIPM machine under the rated state. The materials used in each part of the two machines are all the same, and the rated speed is 1000 rpm. Coupling the loss calculation results of the two-dimensional transient electromagnetic field to the three-dimensional transient temperature field as the heat source, the ambient temperature was set at 22°C. The simulation time is set to 30000 S to make the machine reach a stable state. The temperature cloud diagrams and maximum temperature change curves of the two machines are shown in Figure 19. It can be seen that the temperatures of each part
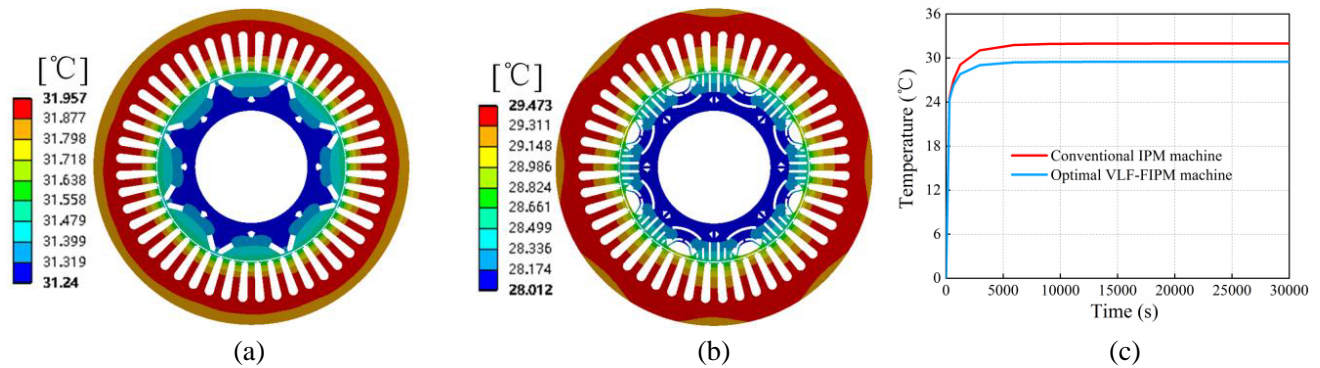
Figure 19. Temperature comparison of the two machines at the rated state. (a) Conventional IPM machine. (b) Optimal VLF-FIPM machine. (c) Maximum temperature change curve of the two machines.
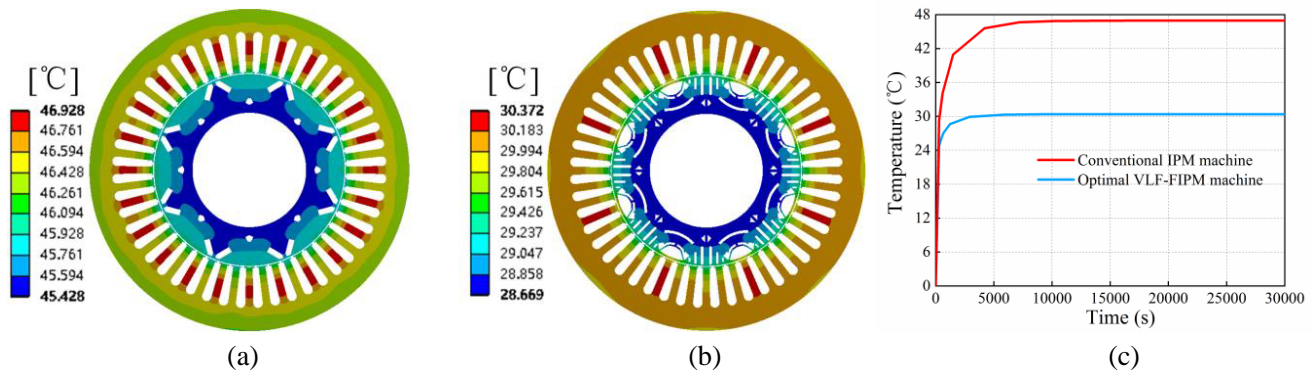

Figure 20. Temperature comparison of the two machines at the limit flux-weakening state. (a) Conventional IPM machine. (b) Optimal VLF-FIPM machine. (c) Maximum temperature change curve of the two machines.

of the two machines are similar, but the temperature of the optimal VLF-FIPM machine is lower. This is due to multiple air magnetic barriers on the rotor of the optimal VLF-FIPM machine, which can increase the overall heat dissipation area of the machine.

Secondly, the temperature fields of the two machines in the limit flux-weakening state are analyzed. The limit speed of the conventional IPM machine is 6600 rpm, while the limit speed of the optimal VLF-FIPM machine is 9400 rpm. Other settings are the same as the rated state. When the temperatures of the two machines reach a stable state, the temperature cloud diagrams and the maximum temperature change curves of the two machines are shown in Figure 20. Compared with the conventional IPM machine, the temperature of the optimal VLF-FIPM machine is significantly reduced in the flux-weakening state, and the maximum temperature difference is about 15°C. Since the optimal VLF-FIPM machine will produce a large amount of inter-pole leakage flux in the flux-weakening state, the core loss of the proposed machine is significantly reduced. Finally, the rationality and effectiveness of the VLF-FIPM machine design are verified.

5.3. Stress Field

There is a large amount of air reluctance on the rotor of VLF-FIPM machine, which will affect the structural stability of the machine, especially at high temperature and high speed. Therefore, this section carries out simulation analysis on the stress and deformation of the rotor of VLF-FIPM machine at 30°C and 10000 rpm. At the same time, the conventional IPM machine is compared to provide objective and fair evaluation.
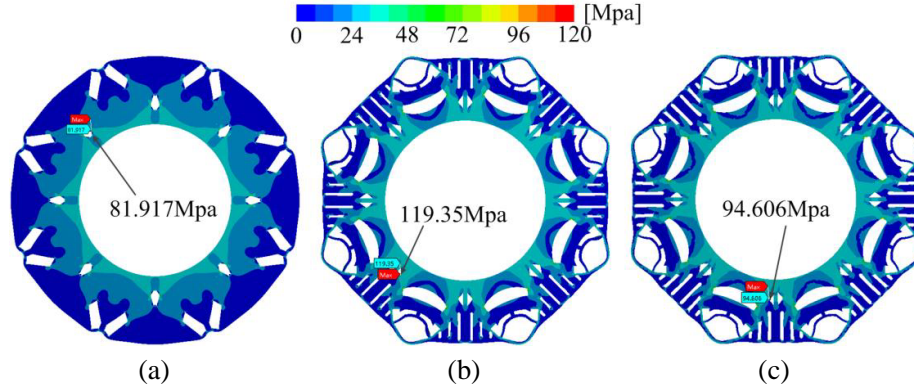
Figure 21. Stress analysis at 30°C and 10000 rpm. (a) Conventional IPM machine. (b) Initial VLF-FIPM machine. (c) Optimal VLF-FIPM machine.
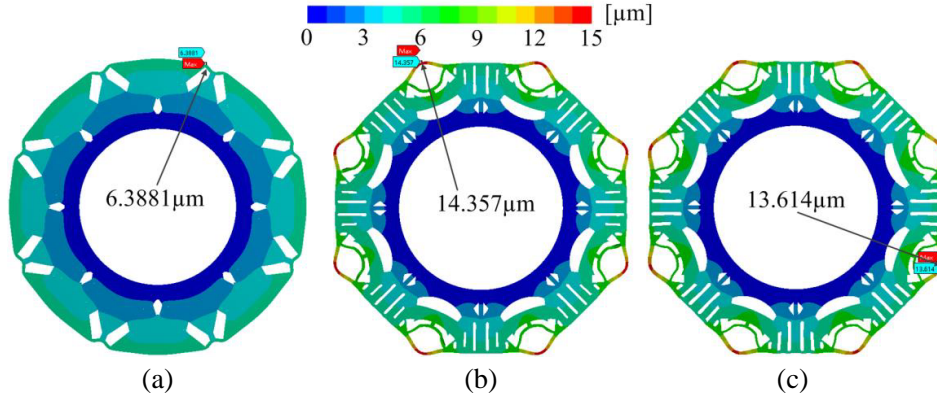

Figure 22. Deformation analysis at 30°C and 10000 rpm. (a) Conventional IPM machine. (b) Initial VLF-FIPM machine. (c) Optimal VLF-FIPM machine.

The stress analysis results of the conventional IPM machine and the initial and optimal VLF-FIPM machines at 30°C and 10000 rpm are shown in Figure 21. After magnifying the stress results, it can be seen that the maximum stresses of the rotors of the three machines all appear at the position of the d-axis magnetic bridge. Although the maximum stress of the optimal VLF-FIPM machine is larger than that of the conventional IPM machine, it is about 25 Mpa less than that of the initial VLF-FIPM machine. Figure 22 shows the deformation results of the rotors of the three machines at 30°C and 10000 rpm. It can be seen from the amplification results that the maximum deformations of the three machines all appear at the edge of the q-axis. The maximum deformation value of the conventional IPM machine is only 6.3881 μm. The maximum deformation value of the VLF-FIPM machine decreases from 14.357 μm before optimization to 13.614 μm after optimization. However, the deformation limit value of the VLF-FIPM machine is 75 μm, which is 1/10 of the air-gap length. Therefore, the optimal VLF-FIPM machine has good mechanical strength at 30°C and 10000 rpm.

6. CONCLUSION

In this article, a new VLF-FIPM machine is introduced, which innovatively combines the variable leakage flux characteristic with the reverse saliency characteristic. Then, a multi-objective comprehensive optimization method is used to improve the output torque and reverse saliency ratio of the proposed machine to a certain extent, and reduce the torque ripple and core loss. The obtained optimal VLF-FIPM machine is compared with the initial VLF-FIPM machine and conventional IPM machine in a comprehensive electromagnetic performance. The results show that the torque ripple of the optimal

VLF-FIPM machine is smaller; the flux-weakening ability is stronger; the PM has a lower risk of irreversible demagnetization in the flux-intensifying state. In addition, the copper losses and core losses of the three machines in the full speed range are compared, and the core loss of the optimal VLF-FIPM machine is lower in the limit flux-weakening state. Finally, the temperature fields of the optimal VLF-FIPM machine in different states are simulated. Compared with the conventional IPM machine, the results show that the temperature of the optimal VLF-FIPM machine is lower in the limit flux-weakening state. The stress and deformation analysis results show that the optimal VLF-FIPM machine has good mechanical strength at $30°C$ and 10000 rpm.

Under the trend of rapid development of EV drive machines, in order to solve the problems of conventional IPM machines such as the difficulty of flux-weakening and speed expansion, the high irreversible demagnetization risk of PM, and the high core loss at high speed, this paper introduces the concepts of variable leakage-flux and flux-intensifying into the machine design, and proposes a new VLF-FIPM machine. The research results also provide a new and feasible way for the design of high-speed machines. This paper combines the single parameter scanning method and multi-objective comprehensive optimization method, which can improve the overall optimization efficiency of multiple design variables, and at the same time make the VLF-FIPM machine exert the best comprehensive performance in EV driving applications. Finally, it also provides a reliable optimization method for the design of a new type of complex structure machine.

ACKNOWLEDGMENT

REFERENCES

1. Dalal, A. and P. Kumar, "Design, prototyping, and testing of a dual-rotor motor for electric vehicle application," *IEEE Transactions on Industrial Electronics*, Vol. 65, No. 9, 7185–7192, 2018.

2. Pellegrino, G., A. Vagati, P. Guglielmi, and B. Boazzo, "Performance comparison between surface-mounted and interior PM motor drives for electric vehicle application," *IEEE Transactions on Industrial Electronics*, Vol. 59, No. 2, 803–811, 2012.

3. Buyukdegirmenci, V. T., A. M. Bazzi, and P. T. Krein, "Evaluation of induction and permanent-magnet synchronous machines using drive-cycle energy and loss minimization in traction applications," *IEEE Transactions on Industry Applications*, Vol. 50, No. 1, 395–403, 2014.

4. Liu, X., H. Chen, J. Zhao, and A. Belahcen, "Research on the performances and parameters of interior PMSM used for electric vehicles," *IEEE Transactions on Industrial Electronics*, Vol. 63, No. 6, 3533–3545, 2016.

5. Huynh, T. A. and M. Hsieh, "Comparative study of PM-assisted SynRM and IPMSM on constant power speed range for EV applications," *IEEE Transactions on Magnetics*, Vol. 53, No. 11, 1–6, 2017.

6. Liu, Y., Z. Zhang, C. Wang, W. Geng, and H. Wang, "Electromagnetic performance analysis of a new hybrid excitation synchronous machine for electric vehicle applications," *IEEE Transactions on Magnetics*, Vol. 54, No. 11, 1–4, 2018.

7. Ding, W., S. Yang, and Y. Hu, "Development and investigation on segmented-stator hybrid-excitation switched reluctance machines with different rotor pole numbers," *IEEE Transactions on Industrial Electronics*, Vol. 65, No. 5, 3784–3794, 2018.

8. Liu, X., M. Wang, D. Chen, and Q. Xie, "A variable flux axial field permanent magnet synchronous machine with a novel mechanical device," *IEEE Transactions on Magnetics*, Vol. 51, No. 11, 1–4, 2015.

9. Sun, T., X. Liu, Y. Zou, C. Huang, and J. Liang, "Design and optimization of a mechanical variable-leakage-flux interior permanent magnet machinewith auxiliary rotatable magnetic poles," *CES Transactions on Electrical Machines and Systems*, Vol. 5, No. 1, 21–29, 2021.

10. Kato, T., M. Minowa, H. Hijikata, K. Akatsu, and R. D. Lorenz, "Design methodology for variable leakage flux IPM for automobile traction drives," *IEEE Transactions on Industry Applications*, Vol. 51, No. 5, 3811–3821, 2015.

11. Athavale, A., T. Fukushige, T. Kato, C. Yu, and R. D. Lorenz, "Variable leakage flux IPMSMs for reduced losses over a driving cycle while maintaining suitable attributes for high-frequency injection-based rotor position self-sensing," *IEEE Transactions on Industry Applications*, Vol. 52, No. 1, 234–241, 2016.

12. Fan, W., X. Zhu, L. Quan, W. Wu, L. Xu, and Y. Liu, "Flux-weakening capability enhancement design and optimization of a variable leakage flux multilayer barrier PM motor," *IEEE Transactions on Industrial Electronics*, Vol. 68, No. 9, 7814–7825, 2021.

13. Limsuwan, N., T. Kato, K. Akatsu, and R. D. Lorenz, "Design and evaluation of a variable-flux flux-intensifying interior permanent-magnet machine," *IEEE Transactions on Industry Applications*, Vol. 50, No. 2, 1015–1024, 2014.

14. Zhu, X., W. Wu, S. Yang, Z. Xiang, and L. Quan, "Comparative design and analysis of new type of flux-intensifying interior permanent magnet motors with different Q-axis rotor flux barriers," *IEEE Transactions on Energy Conversion*, Vol. 33, No. 4, 2260–2269, 2018.

15. Zhu, X., J. Huang, L. Quan, Z. Xiang, and B. Shi, "Comprehensive sensitivity analysis and multiobjective optimization research of permanent magnet flux-intensifying motors," *IEEE Transactions on Industrial Electronics*, Vol. 66, No. 4, 2613–2627, 2019.

16. Sun, X., Z. Shi, G. Lei, Y. Guo, and J. Zhu, "Multi-objective design optimization of an IPMSM based on multilevel strategy," *IEEE Transactions on Industrial Electronics*, Vol. 68, No. 1, 139–148, 2021.

17. Zhou, X., X. Zhu, W. Wu, Z. Xiang, Y. Liu, and L. Quan, "Multi-objective optimization design of variable-saliency-ratio PM motor considering driving cycles," *IEEE Transactions on Industrial Electronics*, Vol. 68, No. 8, 6516–6526, 2021.

18. Du, L., X. Liu, J. Fu, J. Liang, and C. Huang, "Design and optimization of reverse salient permanent magnet synchronous motor based on controllable leakage flux," *CES Transactions on Electrical Machines and Systems*, Vol. 5, No. 2, 163–173, 2021.

19. Si, J., S. Zhao, H. Feng, Y. Hu, and W. Cao, "Analysis of temperature field for a surface-mounted and interior permanent magnet synchronous motor adopting magnetic-thermal coupling method," *CES Transactions on Electrical Machines and Systems*, Vol. 2, No. 1, 166–174, 2018.